Title

Coregistration of diffuse optical spectroscopy and magnetic resonance imaging in a rat tumor model.

Journal

Applied Optics, 42(16)

ISSN

1559-128X

Authors

Merritt, Sean

Bevilacqua, Frederic

Durkin, Anthony J

et al.

Publication Date

2003-06-01

DOI

10.1364/ao.42.002951

Coregistration of diffuse optical spectroscopy and magnetic resonance imaging in a rat tumor model

Sean Merritt, Frederic Bevilacqua, Anthony J. Durkin, David J. Cuccia, Ryan Lanning, Bruce J. Tromberg, Gultekin Gulsen, Hon Yu, Jun Wang, and Orhan Nalcioglu

We report coregistration of near-infrared diffuse optical spectroscopy (DOS) and magnetic resonance imaging (MRI) for the study of animal model tumors. A combined broadband steady-state and frequency-domain apparatus was used to determine tissue oxyhemoglobin, deoxyhemoglobin, and water concentration locally in tumors. Simultaneous MRI coregistration provided structural (T_2-weighted) and contrast-enhanced images of the tumor that were correlated with the optical measurements. By use of Monte Carlo simulations, the optically sampled volume was superimposed on the MR images, showing precisely which tissue structure was probed optically. DOS and MRI coregistration measurements were performed on seven rats over 20 days and were separated into three tumor tissue classifications: viable, edematous, and necrotic. A ratio of water concentration to total hemoglobin concentration, as measured optically, was performed for each tissue type and showed values for edematous tissue to be greater than viable tissue (1.2 ± 0.49 M/μM versus 0.48 ± 0.15 M/μM). Tissue hemoglobin oxygen saturation (StO_2) also showed a large variation between tissue types: viable tissue had an optically measured StO_2 value of $61 \pm 5\%$, whereas StO_2 determined for necrotic tissue was $43 \pm 6\%$.

OCIS codes: 170.5280, 170.6510.

1. Introduction

The development of noninvasive diagnostic techniques to image and characterize physiological properties of tissues is an area of intense research and clinical interest. Such diagnostic tools are crucial for the study of tumor physiology and in particular angiogenesis. Magnetic resonance imaging (MRI) and near-infrared diffuse optical spectroscopy (DOS) are two noninvasive techniques that provide complementary structural and functional physiological information. DOS can be used to measure chromophore concentrations such as oxy- and deoxyhemoglobin (HbO_2 and Hb, respectively), water (H_2O), and fat within a local volume of tissue, whereas MRI provides high-resolution structural and contrast-enhanced images. Coregistration of these two methods has the potential to enhance our understanding of the complex biological processes associated with tumor transformation and growth. Ultimately, the combination of the two measurement techniques can be applied to monitoring tumor changes in response to therapy, resulting in an improved method to test cancer treatment efficacy.[1,2]

The literature documenting the use of MRI to monitor tumor growth and response to therapy is extensive.[3–6] Through the use of MRI contrast agents these studies access functional tissue information, which is key to understanding physiology. For example, several investigations have focused on tumor hypoxia because of the difficulty in treating such tumor tissue clinically.[7,8] The use of perfluorocarbon emulsion as a contrast agent allows for the determination of pO2 values within tissue, enabling elucidation of hypoxic regions.[3] Another example of a widely used contrast agent is Gadopentate dimeglumine (Gd-DTPA), which allows for the determination of vascular volume fraction.[6]

Most of the quantitative DOS studies that have been conducted to date have been performed on breast, brain, and muscle in humans.[9–11] Despite a lower resolution compared with MRI, DOS is attrac-

S. Merritt, F. Bevilacqua, A. J. Durkin, D. J. Cuccia, R. Lanning, and B. J. Tromberg (tromberg@laser.bli.uci.edu) are with the Laser Microbeam and Medical Program, Beckman Laser Institute, University of California Irvine, Irvine, California 92612. G. Gulsen, H. Yu, J. Wang, and O. Nalcioglu (nalci@uci.edu) are with the John Tu and Thomas Yuen Center for Functional Onco-Imaging, University of California Irvine, Irvine, California 92697-5020.

Received 6 September 2002; revised manuscript received 2 December 2002.

0003-6935/03/162951-09$15.00/0

tive because of its direct sensitivity to important physiological parameters such as total hemoglobin content (THC), tissue hemoglobin oxygen saturation (StO_2), fat, and H_2O content. Moreover, its implementation is relatively inexpensive.

The majority of the research reported in the literature that combines DOS and MRI modalities has been carried out in the area of functional brain imaging.[12–16] The main goals of these investigations have been either to validate DOS measurements or to explain the origin of the blood oxygen level dependent signal in functional MRI. For cancer studies, there have been only a few reports of DOS and MRI coregistration.[17–21] Ntziachristos *et al.* developed a diffuse optical tomography/spectroscopy (DOT/DOS) breast-imaging instrument to be used for coregistration with MRI.[17] Their optical system acquires time-resolved data at up to three wavelengths in the near-infrared region. Recently they reported what is believed to be the first clinical application of MR-guided DOS to breast measurements.[20]

When DOT/DOS technology is used as a standalone method, the resolution of the images is limited by the diffusive behavior of light propagating in highly scattering media. Pogue and Paulsen proposed to use *a priori* information from MR images to constrain the image reconstruction of DOT and were able to demonstrate such an approach with simulated data.[21] A MR image of a rat cranium was used to construct a finite-element grid, which segmented brain, bone, and muscle and used literature-reported absorption and scattering coefficients at 800 nm for these different tissue types. The grid was used to simulate DOT measurements using 16 sources and 16 detectors with noise added. Reconstruction assuming only knowledge of the external boundary resulted in low-resolution images, whereas reconstruction using the segmented boundaries obtained from MRI resulted in higher-resolution images.

These prior studies highlight the interest in performing MRI and DOS measurements in parallel. First, the MR images are of help in interpreting the optical data by providing relatively high-resolution structural and functional images. Partial validation of the optical measurements is thus possible. Second, the incorporation of the high-resolution structural information can significantly improve the accuracy of DOT reconstruction. Of course, constraining DOT optimization based on MRI data provides useful images only if the MR contrast elements can be accurately correlated with tissue optical properties.

Here we present the results from an investigation of the correlation between MRI and DOS data as obtained from an *in vivo* rat tumor model. First, we describe the instrumentation used for MRI/DOS coregistration. Second, we report measurements on subcutaneous tumors in rats, periodically measured over an interval of 20 days as tumors developed and changed in structure. DOS measured HbO_2, Hb, and H_2O concentration are compared with both structural MR images (T_2 weighted) and Gd-DTPA contrast-enhanced MR images. A complementary investigation in which both MR and optical contrast agents were employed is described in a companion paper in this issue.[22]

2. Materials and Methods

A. Diffuse Optical Spectroscopy

1. Instrumentation

We used a combined frequency-domain (FD) and steady-state (SS) system that has previously been described in detail.[23] At the core of the FD instrument is a network analyzer (HP 8753C), which is used to modulate the intensity of diode lasers and to measure the phase and amplitude of the optical signal detected by an avalanche photodiode (Hamamatsu APD C556P-56045-03). Five diode lasers at varying wavelengths of 674, 800, 849, 898, and 915 nm were used and were modulated from 50 to 601 MHz sweeping a total of 233 frequencies. The SS instrument is composed of a tungsten–halogen light source (Ocean Optics LS-1) and a spectrometer (Ocean Optics S2000). As explained in Section 2.A.2, the combination of FD and SS data allows for the determination of the broadband absorption spectrum of the tissue (typically 650–1000 nm).

The optical instrument was housed in a room separate from the MR imager in order to reduce problems associated with the 3-T magnet. This requirement necessitated the use of 20-m lengths of optical fiber to conduct light from the diode lasers and tungsten light source to the probe, which was located inside the bore of the magnet; the diffuse light was then collected by detector fibers of equal length and relayed back to the detectors. Such fiber length does not significantly affect SS measurements but is problematic for FD measurements because of modal dispersion of the fibers. To overcome such a problem, we used 100-μm core diameter, 3-mm outer diameter 100/140 cabled, gradient-index fiber (OZ Optics MMJ-3X-IRVIS-100/140-3-40) for the source fiber and 600-μm core diameter, 1.1-mm cladding diameter, gradient-index fiber, for the detector fiber (Oxford Electronics). Note that this latter fiber is not commonly commercially available but is a custom item. For the SS measurements, we used 600-μm core diameter step-index fibers for both the source and detector.

The optical probe was made of Delrin acetal resin and included a head, which rested on the tumor. The probe head was a 1-in.- (2.54-cm-) diameter cylinder with holes drilled through lengthwise for placement of the source and detector fibers. The source and detector fibers were inserted into the drilled holes and fixed in place flush with the probe head with epoxy. Plastic rings filled with $H_2O \cdot CuSO_4$ solution, placed around the probe, allow for the determination of the location of the source and detector fibers in the MR images.[17,18]

For the FD measurements, amplitude and phase were calibrated by use of a silicone phantom with

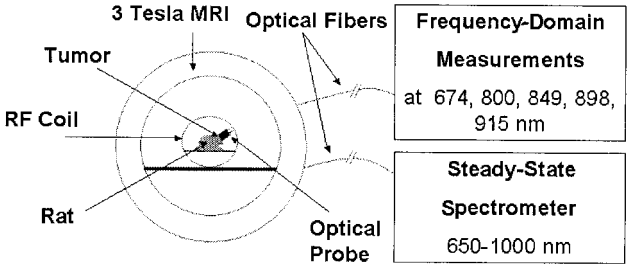

Fig. 1. Experimental setup of MRI and NIRS instruments.

previously characterized optical properties.[24] For the SS measurements, an integrating sphere was used to calibrate the spectral instrument response.

2. *Optical Property Determination*

The method used to determine the optical properties is explained in detail by Bevilaqua *et al.*[23] The computations are based on the analytical diffusion solution of the reflectance $R[\mu_a(\lambda), \mu_s'(\lambda), f]$ given by Kienle and Patterson, where $\mu_a(\lambda)$ is the absorption coefficient, $\mu_s'(\lambda)$ is the reduced-scattering coefficient, and f is the modulation frequency.[25] The same analytical solution is valid for SS ($f = 0$) and FD data.[23] First, $\mu_a(\lambda)$ and $\mu_s'(\lambda)$ are obtained at the laser-diode wavelengths from the fit of the diffusion solution to the calibrated phase and amplitude. Assuming μ_s' to have the form $\mu_s'(\lambda) = A\lambda^{-B}$, we can obtain the broadband scattering spectrum by fitting the $\mu_s'(\lambda)$ values at the laser-diode wavelengths to the above equation.[26–28] The $\mu_a(\lambda)$ and $\mu_s'(\lambda)$ values at the laser wavelengths obtained from FD measurements are also used to calibrate the broadband reflectance spectrum obtained from SS measurements, again by use of diffusion theory. Note that this calibration step corresponds only to the determination of a single scaling factor that allows for the determination of the absolute reflectance spectrum $R(\lambda)$ expressed in [W/m^2]. The last step is to determine the broadband absorption spectra $\mu_a(\lambda)$ from the broadband absolute reflectance spectra $R(\lambda)$ and the broadband $\mu_s'(\lambda)$ spectrum, with the diffusion solution a third time. Finally, concentrations of Hb, HbO_2, and H_2O are determined by a linear least-squares fit of the absorption spectra of the chromophores to the measured absorption spectrum over the 650–1000-nm wavelength range. Although our DOS instrument also has the ability to determine lipid concentrations, the rat tumor tissues measured contained insignificant amounts of fat and did not necessitate the use of the fat spectrum in the chromophore fit.

3. *Magnetic Resonance Imaging Instrument and Methodology*

Figure 1 illustrates how DOS measurements are obtained within the MRI. The homebuilt MRI system has a 3.0-T magnet and uses a Marconi medical console. The bore diameter of the MRI is 90 cm, and a homebuilt, small-animal, birdcage-type rf coil is used to transmit and receive signals.

For the study, two types of MRI images were obtained. First, T_2-weighted images using a fast spin-echo sequence [(TR/TE), 3000/105 ms; field of view, 14 cm; slice thickness, 5 mm; image matrix, 256 × 256; echo train, 8] were acquired over the whole tumor for the anatomical information. The acquisition time for the T_2 images was 3 min.

The second type of images acquired were from a T_1-weighted dynamic acquisition based on a fast three-dimensional gradient echo pulse sequence (TR/TE, 18/3.6 ms; flip angle, 20°; field of view, 10.5; slice thickness, 5 mm; image matrix, 256 × 256) in which 40 sequential images were acquired over a 16-min time period (24.1 s/image). A bolus injection of Gd-DTPA (0.1 mmol/kg) was administered after the first four images (baseline measurements) in this T_1-weighted acquisition. Gd-DTPA–induced enhancement images for the tumor were then constructed by means of subtracting the average intensity of the four baseline images from each subsequent dynamic image after the Gd-DTPA injection. Since only one T_1-weighted measurement, following bolus injection, was used for the enhancement images, we chose the same time point for all the tumor measurements in order for our analysis to be consistent. Although the uptake of the Gd-DTPA varied for each tumor, the fifth of the 40 consecutive time points (120 s after injection) supplied a sufficient amount of contrast agent signal for the analysis of all tumors.

B. Sampling Volume Visualization

To visualize the coregistration of DOS with MRI measurements, development of a means for overlaying the optical and MR sampling volumes is essential. DOS measurements are used to determine values of μ_a and μ_s' over a volume of tissue, the dimensions of which depend on both the source–detector separation and the average optical properties of the sampled region. Maps constructed from the results of Monte Carlo (MC) simulations based on measured average transport parameters provide a means to visualize the optically probed region that can be superimposed on MR images.[29–33]

Although the same treatment can be performed with a diffusion-based model, the weighting of the map near the source and detector are inaccurate and lead to pronounced errors over the entire volume for the relatively short source–detector separation (5.7 mm) used. The MC map describes the probability for a detected photon to have traveled through a given voxel.

The input parameters used in the generation of the MC maps included the modulation frequency, the source–detector separation, and the measured optical coefficients μ_a, μ_s'. As a first approach we considered the portion of tissue investigated optically as homogeneous. The validity of such an assumption is discussed in Section 3.

Strictly speaking, a MC map is generated for each modulation frequency and a given wavelength, since the optical properties of tissue depend on the wavelength. However, for the purposes of this investiga-

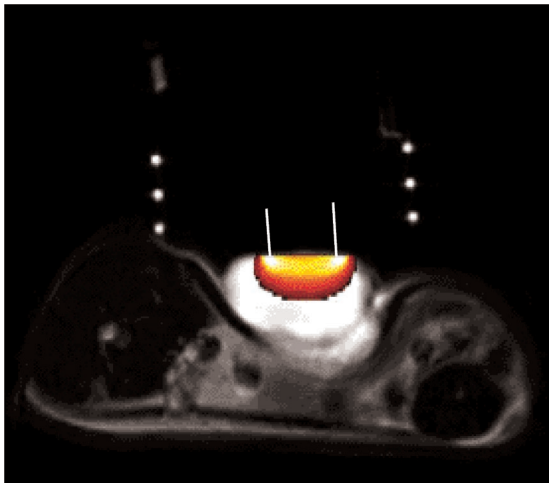

Fig. 2. Example of T_2-weighted MRI of rat cross section with MC map superimposed on image. Six white dots above the rat are cross sections of three $H_2O \cdot CuSO_4$ filled tubes that wrap around probe. The markers determine the location of the source and detector fibers, separated by 5.7 mm. The input parameters for MC map are $\mu_a = 0.015\ mm^{-1}$, $\mu_s' = 1.30\ mm^{-1}$, and modulation frequency of 300 Mhz.

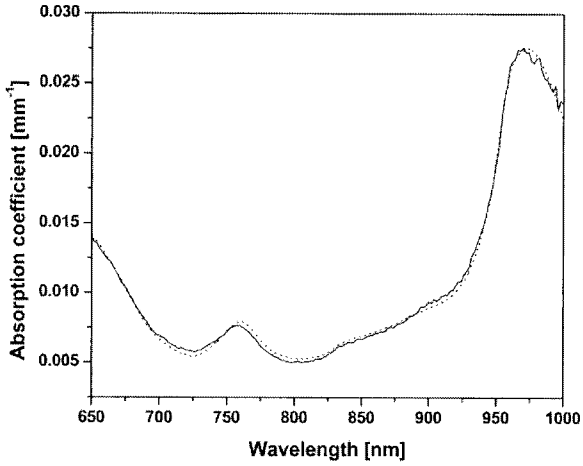

Fig. 3. Solid curve, μ_a tumor spectrum measured optically with DOS instrument. Dashed curve, fit of Hb, HbO_2, H_2O, and baseline absorption spectra to measured μ_a spectrum.

tion, we determined that the frequency- and wavelength-dependent variations in interrogated tissue volumes were not significant for the relatively small source–detector separation (5.7 mm) used in this study. The mean depth probed by the light, for an average $\mu_a = 0.015\ mm^{-1}$ and modulation frequency of 300 MHz, changed by less that 4% over the frequency range of 50–600 MHz. For absorption variations the mean depth probed changed by ~20% for $\mu_a = 0.08\ mm^{-1}$ and $\mu_a = 0.005\ mm^{-1}$, which were the maximum and minimum absorption values of all the measurements and therefore represent a larger deviation than for a single measurement. In view of these small differences, the maps were generated with only the average optical properties from each respective measurement and a modulation frequency of 300 MHz.

After the MC maps were constructed by use of the optical properties measured for a particular tumor, they were then aligned with the MR images by use of the pixel locations determined for the source and detector fibers. The $H_2O \cdot CuSO_4$ filled markers placed on the optical probe's head were used to define the pixel location of the optical source and detector fibers on the T_2 image. MC maps could then be superimposed on the MR images and define the region probed optically. Figure 2 shows a typical example of a superposition of the MC map over a MR image.

C. Animal Protocol and Coregistration

A group of seven female Fisher-344 rats (weight range, 170–210 g) were implanted with the R3230 AC adenocarcinoma tumor model 2 wk prior to being subject to a series of DOS and MRI measurements. The acquisition of data was initiated when tumor sizes reached 1 cm in diameter. Data acquisition continued until tumors reached a maximum size of 3 cm in diameter. Each rat was measured every 3–5 days, excluding any unavoidable circumstances, over a period of 20 days for a total of 26 measurements. All procedures followed a protocol approved by the Institutional Animal Care and Use Committee of the University of California, Irvine (IACUC Protocol 2002-2323-0).

The DOS measurements were performed during the acquisition of MRI measurements. For a given measurement session, a rat was placed inside the rf coil, and the head of the optical probe was placed in contact with the tumor. T_2 images were acquired to locate the tumor and the $H_2O \cdot CuSO_4$-filled markers were used to indicate the location of the optical source and detector fibers relative to the tumor. DOS data were acquired three times during the acquisition of the T_2 images. Three additional DOS measurements were recorded after the Gd-DTPA bolus injection, during the acquisition of the T_1 measurements. The six measurements were averaged, and error bars were calculated with the standard deviation of all measurements. There were no consistent differences in optical data taken before and after measurements; therefore the MRI contrast agent did not appear to perturb the absorption and scattering events of the light, either directly or as a consequence of blood dilution.

3. Results and Discussion

Figure 3 shows a typical μ_a spectrum measured on the rat tumor, as computed from the FD and SS measurements explained in Subsection 2.A.2. The fit of the chromophore spectra (Hb, HbO_2, H_2O, and constant background absorption) to the μ_a spectrum allows for the determination of the concentrations. The background absorption is on average 8% of the total absorption spectrum for all measurements. It may account for background chromophores other than Hb, HbO_2, and H_2O with no significant spectral features or in trace amounts. Nevertheless, the

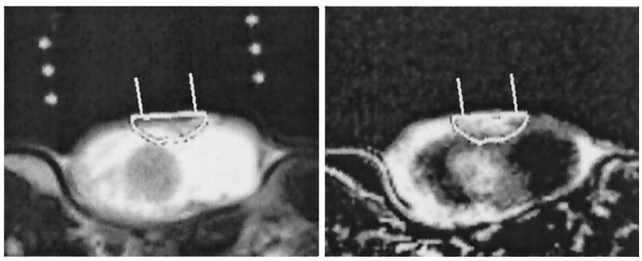

(a) (b)

Fig. 4. Example of (a) T_2 and (b) enhancement image for viable tissue. The source and detector fibers (5.7-mm separation) are represented by white bars on tumors. Area within white MC contour line represents 75% weight of MC map. Optical measurements: $H_2O = 30 \pm 0.4$ M, THC $= 61 \pm 0.6$ μM, $StO_2 = 62 \pm 0.5\%$.

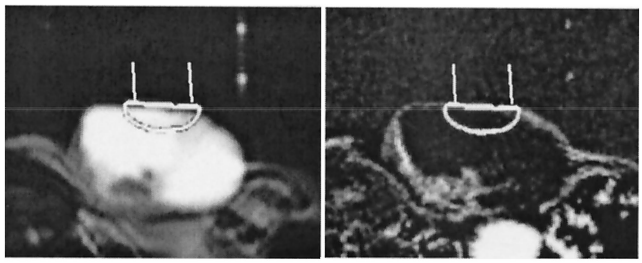

(a) (b)

Fig. 5. Example of (a) T_2 and (b) enhancement image for edematous tissue. Source–detector distance and contour line are as in Fig. 4. Optical measurements: $H_2O = 102 \pm 2$ M, THC $= 66 \pm 2$ μM, $StO_2 = 64 \pm 2\%$.

background absorption also serves to correct for a systematic offset in the absorption value that is due to both model inaccuracy and calibration inaccuracy. Previous research in tissue phantoms showed that, in the case of a broadband absorption spectrum, adding this degree of freedom in the fit can significantly improve its accuracy.[34]

Figure 3 illustrates the quality of the fit. The various features of Hb and H_2O absorption are clearly visible: high absorption of Hb at 650 nm (peak at 555 nm), peak of Hb at 758 nm, and peak absorption of H_2O at 978 nm.

From the examination of the MC maps superimposed on MR images, as described in the Section 2, we found that the optical measurements were performed essentially on three types of tissue: viable, edematous, and necrotic. This simple classification was intended as a first step toward the understanding of the correlation between optical properties and MR images:

1. *Viable tissue.* Viable tissue was defined by average or high signal (bright regions) of Gd-DTPA on the enhancement image, and normal or low signal (dark regions) in the T_2-weighted image. The signal in the enhancement image is proportional to the perfusion of the Gd-DTPA contrast agent and, therefore, signifies normal or high blood flow to the considered region. The signal in the T_2 image is derived from protons in H_2O and is therefore related to the H_2O concentration measured by DOS. Figure 4 shows an example of a typical (a) T_2 image and (b) enhancement image of viable tissue.

2. *Edematous tissue.* Edematous tissue was defined by a high signal (bright regions) in the T_2 image relative to viable tissue, which corresponds to an increased H_2O concentration. This type of tissue is also characterized by a low enhancement (dark regions) of Gd-DTPA, corresponding to low perfusion or poor blood flow. Figure 5 shows the (a) T_2 and (b) enhancement images for a typical example of edematous tissue. The formation of such edematous structure is commonly found for this type of tumor animal model.

3. *Necrotic tissue.* Necrotic tissue was defined by normal T_2 intensity and low Gd-DTPA enhancement, corresponding to low perfusion of blood. MRI therefore suggests a tissue that has normal H_2O content but poor blood supply. Figure 6 shows the (a) T_2 and (b) enhancement images for a typical example of necrotic tissue.

Following the analysis of all measurements for the seven rats over the 20-day period, measurements were grouped into these three distinct types of tissue. Figure 7 is a StO_2 versus H_2O scatter plot that includes all measurements. The average chromophore concentrations for these three cases are summarized in Table 1. Pham *et al.* have reported comparable rat tumor optical properties.[35] Our main goal here is to assess the optical differences between the various tissue types.

On the basis of H_2O content, viable and necrotic tissue types are clustered together (23 to 36 M). Separation occurs between these two types of tissue as values decrease in StO_2 (Fig. 7). Necrotic tissue shows significantly lower tissue StO_2 ($43\% \pm 6\%$) compared with viable ($61\% \pm 5\%$) and a lower mean THC than viable tissues (51 ± 8 μM versus 64 ± 19 μM). These results are consistent with expected physiological differences.[36]

The measurements performed on the edematous

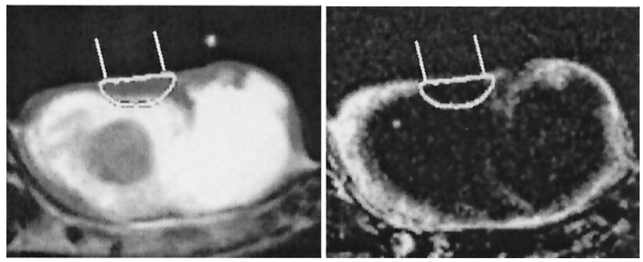

(a) (b)

Fig. 6. Example of (a) T_2 and (b) enhancement image for necrotic tissue. Source–detector distance and contour line are as in Fig. 4. Optical measurements: $H_2O = 31 \pm 0.3$ M, THC $= 45 \pm 1$ μM, $StO_2 = 51 \pm 2\%$.

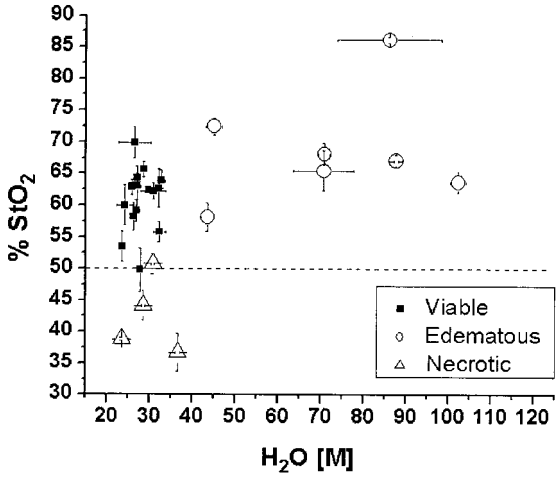

Fig. 7. All optical measurements determined from SS-FD data plotted on graph of StO_2 versus H_2O. The three tissue types as identified by MRI are separated clearly on the plot: edematous tissue (○), viable tissue (■), and necrotic tissue (△).

tissue separate clearly from all other measurements because of the high relative H_2O concentration measured. In Fig. 7, two edematous cases are located close to the viable tissue cluster. Interestingly, in these cases the MC map overlapped both an edematous and a viable region, which confirms that these measurements can be considered to be mixed cases.

The values of H_2O concentration calculated in edematous tissue (84 ± 13 M) exceed physical plausibility (~160% H_2O). This problem most likely results because the edematous cases are composed of a low-scattering mixture consisting of mostly H_2O. Such a tissue type may easily challenge the validity of our diffusion model, especially at the short source–detector separation used (5.7 mm). Qualitatively, the optical measurements provide the correct trend, i.e., high H_2O concentration, but the values are quantitatively inaccurate.

For the same reasons that the measured H_2O concentrations of edematous tissue are quantitatively inaccurate, THC values reported in Table 1 are also inaccurate. When the μ_a spectrum was determined, it was shifted up for the edematous cases, which led to the high H_2O concentrations when the chromophore fit was performed. This shift in the μ_a spectrum would also explain the high average THC value for the edematous cases listed in Table 1. To ensure that the shifted spectrum does indeed have a higher H_2O content, Table 2 lists the ratio H_2O [M] to THC [μM] for the three different tissue types. As expected, the edematous cases have the highest ratios and the viable cases have the lowest ratios confirming the higher H_2O concentrations in the edematous tissue as measured by DOS.

Table 1. Chromophore Values Measured Optically for Different Tissue Types[a]

Tissue Type	H_2O [M]	THC [μM]	StO_2 [%]
Viable	28 ± 3	64 ± 19	61 ± 5
Edematous	84 ± 13	76 ± 32	70 ± 9
Necrotic	30 ± 5	51 ± 8	43 ± 6

[a]Errors are given by standard deviation of multiple measurements taken. The number of measurements taken on viable, edematous, and necrotic tissue types was 15, 7, and 4, respectively.

Table 2. Ratio of H_2O [M] to THC [μM] for Different Tissue Types

Tissue Type	H_2O [M]/THC [μM]
Viable	0.48 ± 0.15
Edematous	1.2 ± 0.49
Necrotic	0.60 ± 0.09

For optical properties characteristic of viable and necrotic tissues, we and others have shown that the approximations is valid, even if the source–detector separation used is relatively small (5.7 mm).[37,38] Kienle and Patterson demonstrated indeed that retrieval of μ_a with $\mu_s' = 1$, at a single distance of 6 mm and a modulation frequency of 195 MHz resulted in an error less that 10% when the μ_a value to be determined was less than 0.02 mm^{-1} (Ref. 38). We also performed a validation study on a phantom at a range of source–detector separations to test the limits of our instrument's ability to extract the correct optical coefficients and found similar errors for a distance of 5.7 mm. It is important to note that the ability to determine a broadband absorption spectrum, by use of both SS and FD techniques, is essential in this study. Using only the limited set of wavelengths of the FD measurements (674, 800, 849, 898, and 915 nm) would dramatically increase the errors in the determination of chromophore concentrations. More precisely, the uncertainty in a measurement set, defined as the standard deviation of consecutive measurements divided by the average measured value, increases by 3-fold for Hb and HbO_2 and 18-fold for H_2O when the steady-state measurement was not included. Moreover, the accuracy of the measurement set also deteriorates and correlation with MRI is not possible.

This confirms our previous findings that the broadband absorption spectrum allows for significantly more accurate and precise values of the chromophore concentrations.[10,23,34]

Finally, we present an example of a time course measurement on a single tumor followed over a 20-day period. Figure is 8(a), 8(b), and 8(c) show the MR T_2-weighted images obtained on day 1, 11, and 20, respectively. Figure 8(d) illustrates the StO_2, THC, and H_2O concentration calculated from optical measurements for the same tumor. The MRI T_2-weighted images show that dramatic changes occur in the tumor structure that are consistent with the optical measurements. The sharp increase of H_2O for the measurement acquired on day 11 is consistent with the T_2 image on that day exhibiting a strong signal, indicating high H_2O content. Furthermore, measurements taken during the first 11 days show the tumor to have StO_2 values greater than 50%,

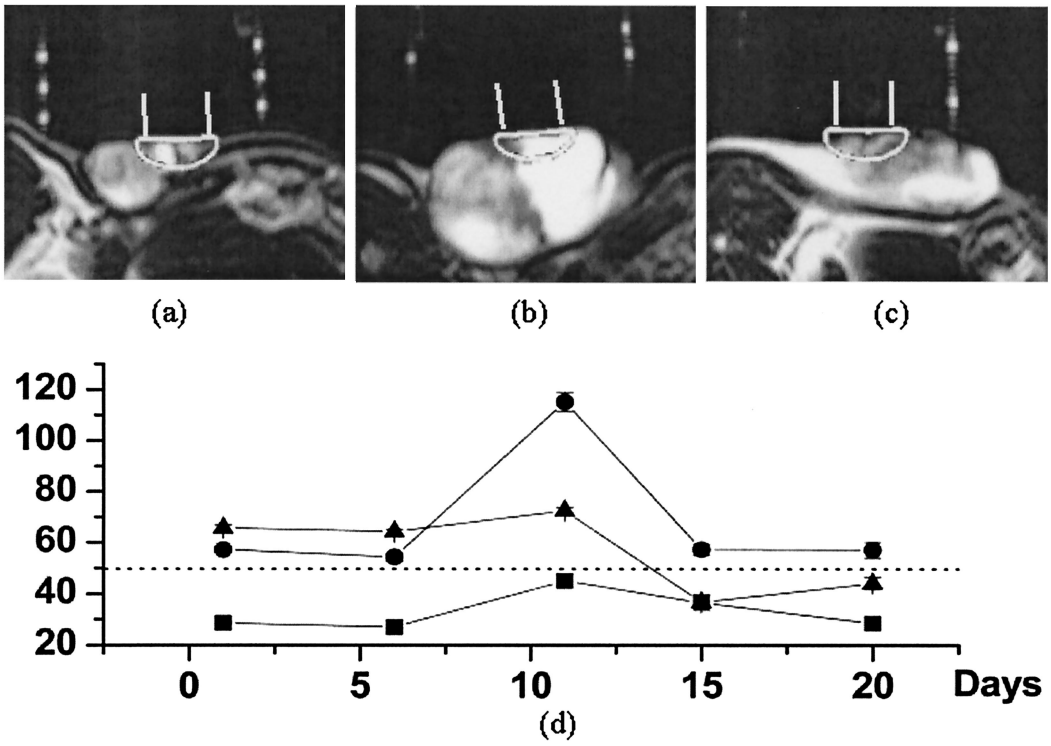

Fig. 8. T_2-weighted images of a rat tumor for days (a) 1, (b) 11, and (c) 20. Source–detector distance and contour line are as in Fig. 4 for each image. Chromophore values for the same rat tumor in (a), (b), and (c) are plotted for all optical measurements over the 20-day period in (d). H_2O values (●) are measured in molars, StO_2 values (▲) in percentage, and THC values (■) in micromolars.

whereas the final two time points show a measured StO_2 of less that 50%. From this we observe the tumor becoming more necrotic over time at the position of the measurements, which was generally true for all tumors in this study. However, the overall temporal evolution of the tumors varied greatly between each rat, with the formation of edematous tissue occurring at various times. Therefore MRI coregistration was essential to explain and validate time variations found in the optical measurements.

4. Conclusion

The integration of a first-generation steady-state (SS) and frequency-domain (FD) photon migration instrument with MRI has been realized. This new instrument allows for the local quantitative investigation of tissue properties on the rat tumor while MRI is simultaneously performed. Coregistration of the DOS and MRI systems was achieved by means of superimposing Monte Carlo simulations defining the path taken by photons over the MR image. Analysis was then performed to correlate the MR images with optical measurements of chromophore concentrations.

Results from the optical measurements on subcutaneous adenocarcinoma tumors in a rat model were obtained and coregistered with MRI data. Analysis of the structural T_2-weighted images and functional Gd-DTPA-enhanced regions were compared with physiological parameters derived from the optical measurements. Tissues were separated into three types based on the MR images: viable, edematous, and necrotic. This classification was in agreement with the physiological parameters derived from optical measurements. Edematous tissue exhibited high H_2O concentrations, and necrotic tissue measurements showed a significant decrease in both THC and StO_2. The successful correlation between the DOS and MRI systems was possible because of the broadband spectroscopic capabilities of the SS-FDPM instrument. Rather than attempting to correlate absorption and scattering coefficient with MRI at a few accessible wavelengths, our system provides the ability to compare absolute chromophore concentrations with the MRI measurements.

To our knowledge, Kuboki *et al.* performed the only previous study comparing DOS data with T_2-weighted MRI data.[39] They acquired data before, during, and after clenching of the masseter muscle in humans with both DOS and MRI technology. Because their DOS instrument was able to acquire only Hb and HbO_2 concentrations, they compared changes in THC with signal intensity changes in T_2 images. They argue that because H_2O is the predominant component of blood, THC changes are related to H_2O changes as measured by MRI. Unfortunately, they acquired DOS and MRI data on separate days out of necessity, but they were still able to correlate signals. Because of its broad spectral coverage, our instrument provides the benefit of a direct correlation between DOS and MRI for both H_2O and lipid, and T_1-weighted contrast-enhanced MRI for THC.

Although our main focus in this research was to correlate optical and MRI signals, the study also helps to establish a basis for the use of relatively inexpensive, portable DOS technologies in animal tumor models. Interestingly, few studies using DOS have been reported on animal tumors.[35,40–42] In contrast, substantial effort has been dedicated to small-animal model functional imaging by researchers using other noninvasive strategies such as MRI and positron emission tomography (micro-PET).[3–6,43] Our results suggest that DOS is a viable complementary, and in some uses alternative, approach to radiological methods for noninvasive tumor functional imaging. Future studies will focus on advancing the optics instrumentation by adding optical tomographic capabilities.

This research was supported by National Institutes of Health grants RR01192 (Laser Microbeam and Medical Program, LAMMP) and NIH P20-CA86182; the Department of Energy (DOE DE-FG03-91ER61227), and the Avon Foundation—Chao Family Cancer Center. A. J. Durkin acknowledges Michael Berns and the Beckman Foundation for fellowship support. D. J. Luccia acknowledges a summer fellowship provided by the Undergraduate Research and Opportunities Program (UROP) at the University of California, Irvine (UCI).

References

1. R. G. Steen, D. A. Wilson, C. Bowser, J. P. Wehrle, J. D. Glickson, and S. S. Rajan, "^{31}P NMR Spectroscopic and near infrared spectrophotometric studies of effects of anesthetics on *in vivo* RIF-1 tumors. Relationship to tumor radiosensitivity," NMR Biomed. **2,** 87–92 (1989).
2. D. B. Jakubowski, A. E. Cerussi, F. Bevilacaua, N. Shah, D. Hsiang, J. Butler, and B. J. Tromberg, Beckman Laser Institute, University of California at Irvine, 1002 Health Sciences Road, Irvine, Calif. 92612, are preparing a manuscript to be called "Monitoring neoadjuvant chemotherapy in breast cancer using quantitative diffuse optical spectroscopy: a case study."
3. Z. Wang, M.-Y. Su, and O. Nalcioglu, "Applications of dynamic contrast enhanced MRI in oncology: measurement of tumor oxygen tension," Technol. Cancer Res. Treat. **1,** 29–38 (2002).
4. R. P. Mason, A. Constantinescu, S. Hunjan, D. Le, E. W. Hahn, P. P. Antich, C. Blum, and P. Peschke, "Regional tumor oxygenation and measurement of dynamic changes," Radiat. Res. **152,** 239–249 (1999).
5. D. Zhao, A. Constantinescu, E. W. Hahn, and R. P. Mason, "Tumor oxygen dynamics with respect to growth and respiratory challenge: investigation of the dunning prostate R3327-HI tumor," Radiat. Res. **156,** 510–520 (2001).
6. M.-Y. Su, J.-C. Jao, and O. Nalcioglu, "Measurement of vascular volume fraction and blood-tissue permeability constants with a pharmacokinetic model: studies in rat muscle tumors with dynamic Gd-DTPA enhanced MRI," Magn. Reson. Med. **32,** 714–724 (1994).
7. M. Höckel, K. Schlenger, B. Aral, M. Mitze, U. Schäffer, and P. Vaupel, "Association between tumor hypoxia and malignant progression in advanced cancer of the uterine cervix," Cancer Res. **56,** 4509–4515 (1996).
8. J. M. Brown, "The hypoxic cell: a target for selective cancer therapy," Cancer Res. **59,** 5863–5870 (1999).
9. T. Sako, T. Hamaoka, H. Higuchi, Y. Kurosawa, and T. Katsumura, "Validity of NIR spectroscopy for quantitatively measuring muscle oxidative metabolic rate in exercise," J. Appl. Physiol. **90,** 338–344 (2001).
10. A. E. Cerussi, D. Jakubowski, N. Shah, F. Bevilacqua, R. Lanning, A. J. Berger, D. Hsiang, J. Butler, R. F. Holcombe, and B. J. Tromberg, "Spectroscopy enhances the information content of optical mammography," J. Biomed. Opt. **7,** 60–71 (2002).
11. M. Kohl-Bareis, H. Obrig, J. Steinbrink, J. Malak, K. Uludag, and A. Villringer, "Noninvasive monitoring of cerebral blood flow by a dye bolus method: separation of brain from skin and skull signals," J. Biomed. Opt. **7,** 464–470 (2002).
12. A. Kleinschmidt, H. Obrig, M. Requardt, K.-L. Merboldt, U. Dirnagl, A. Villringer, and J. Frahm, "Simultaneous recording of cerebral blood oxygenation changes during human brain activation by magnetic resonance imaging and near-infrared spectroscopy," J. Cereb. Blood Flow Metab. **16,** 817–826 (1996).
13. V. Toronov, A. Webb, J. H. Choi, M. Wolf, A. Michalos, E. Gratton, and D. Hueber, "Investigation of human brain hemodynamics by simultaneous near-infrared spectroscopy and functional magnetic resonance imaging," Med. Phys. **28,** 521–527 (2001).
14. Y. Xie, K. Sakatani, W. Lichty, H. Zuo, Z. Xie, and J. Bai, "Near-infrared spectroscopy studies on cerebral blood oxygenation changes during brain activation: possible limitations of blood oxygenation level dependent functional magnetic resonance imaging," Opt. Eng. **40,** 2302–2307 (2001).
15. V. Toronov, A. Webb, J. H. Choi, M. Wolf, L. Safonova, U. Wolf, and E. Gratton, "Study of local cerebral hemodynamics by frequency-domain near-infrared spectroscopy and correlation with simultaneously acquired functional magnetic resonance imaging," Opt. Express **9,** 417–427 (2001), http://www.opticsexpress.org.
16. D. J. Mehagnoul-Schipper, B. F. W. van der Kallen, W. N. J. M. Colier, M. C. van der Sluijs, L. J. Th. O. van Erning, H. O. M. Thijssen, B. Oeseburg, W. H. L. Hoefnagels, and R. W. M. M. Jansen, "Simultaneous measurements of cerebral oxygenation changes during brain activation by near-infrared spectroscopy and functional magnetic resonance imaging in healthy young and elderly subjects," Hum. Brain Map. **16,** 14–23 (2002).
17. V. Ntziachristos, X. H. Ma, and B. Chance, "Time-correlated single photon counting imager for simultaneous magnetic resonance and near-infrared mammography," Rev. Sci. Instrum. **69,** 4221–4233 (1998).
18. V. Ntziachristos, A. G. Yodh, M. Schnall, and B. Chance, "Concurrent MRI and diffuse optical tomography of breast after indocyanine green enhancement," Proc. Natl. Acad. Sci. USA **97,** 2767–2780 (2000).
19. V. Ntziachristos, A. H. Hielscher, A. G. Yodh, and B. Chance, "Diffuse optical tomography of highly heterogeneous media," IEEE Trans. Med. Imaging **20,** 470–478 (2001).
20. V. Ntziachristos, A. G. Yodh, M. D. Schnall, and B. Chance, "MRI-guided diffuse optical spectroscopy of malignant and benign breast lesions," Neoplasia **4,** 347–354 (2002).
21. B. Pogue and K. D. Paulsen, "High-resolution near-infrared tomographic imaging simulations of the rat cranium by use of *a priori* magnetic resonance imaging structural information," Opt. Lett. **23,** 1716–1718 (1998).
22. D. J. Cuccia, F. Bevilacqua, A. J. Durkin, S. Merritt, B. J. Tromberg, G. Gulsen, H. Yu, J. Wang, and O. Nalcioglu, "*In vivo* quantification of optical contrast agent dynamics in rat tumors by use of diffuse optical spectroscopy with magnetic resonance imaging coregistration," Appl. Opt. **42,** 2940–2950 (2003).
23. F. Bevilacqua, A. J. Berger, A. E. Cerussi, D. Jakubowski, and B. J. Tromberg, "Broadband absorption spectroscopy in turbid media by combined frequency-domain and steady-state methods," Appl. Opt. **39,** 6498–6507 (2000).

24. T. Pham, O. Coquoz, J. B. Fishkin, E. Anderson, and B. J. Tromberg, "Broad bandwidth frequency domain instrument for quantitative tissue optical spectroscopy," Rev. Sci. Instrum. **71,** 2500–2513 (2000).
25. A. Kienle and M. S. Patterson, "Improved solutions of the steady-state and the time-resolved diffusion equations for reflectance from a semi-infinite turbid medium," J. Opt. Soc. Am. A **14,** 246–254 (1997).
26. R. Graaff, J. G. Aarnoudse, J. R. Zijp, P. M. A. Sloot, F. F. M. de Mul, J. Greve, and H. M. Koelink, "Reduced light-scattering properties for mixtures of spherical particles: a simple approximation derived from Mie calculations," Appl. Opt. **31,** 1370–1376 (1992).
27. J. M. Schmitt and G. Kumar, "Optical scattering properties of soft tissue: a discrete particle model," Appl. Opt. **37,** 2788–2797 (1998).
28. J. R. Mourant, J. P. Freyer, A. H. Hielscher, A. A. Eick, D. Shen, and T. M. Johnson, "Mechanisms of light scattering from biological cells relevant to noninvasive optical-tissue diagnostics," Appl. Opt. **37,** 3586–3593 (1998).
29. M. S. Patterson, S. Andersson-Engels, B. C. Wilson, and E. K. Osei, "Absorption spectroscopy in tissue-simulating materials: a theoretical and experimental study of photon paths," Appl. Opt. **34,** 22–29 (1995).
30. E. Okada, M. Firbank, M. Schweiger, S. R. Arridge, M. Cope, and D. T. Delpy, "Theoretical and experimental investigation of near-infrared light propagation in a model of the adult head", Appl. Opt. **36,** 21–31 (1997).
31. E. M. Sevick, J. K. Frisoli, C. L. Burch, and J. R. Lakowicz, "Localization of absorbers in scattering media by use of frequency-domain measurements of time-dependent photon migration," Appl. Opt. **33,** 3562–3570 (1994).
32. F. Bevilacqua, J. S. You, B. J. Tromberg, and V. Venugopalan, "Sampling of tissue volume by frequency-domain photon migration," in *Biomedical Topical Meetings*, Vol. 38 of OSA Trends in Optics and Photonics Series (Optical Society of America, Washington, D.C., 2000), pp. 78–80.
33. D. A. Boas, J. P. Culver, J. J. Stott, and A. K. Dunn, "Three dimensional Monte Carlo code for photon migration through complex heterogeneous media including the adult human head," Opt. Express **10,** 159–170 (2002), http://www.opticsexpress.org.
34. D. B. Jakubowski, "Development of broadband quantitative tissue optical spectroscopy for the non-invasive characterization of breast disease," Ph. D. dissertation (University of California, Irvine, Irvine, Calif., 2002).
35. T. H. Pham, R. Homung, M. W. Berns, Y. Tadir, and B. J. Tromberg, "Monitoring tumor response during photodynamic therapy using near-infrared photon-migration spectroscopy," Photochem. Photobiol. **73,** 669–677 (2001).
36. *Dorland's Illustrated Medical Dictionary* (Saunders, Philadelphia, 1994).
37. F. Bevilacqua and C. Depeursinge, "Monte Carlo study of diffuse reflectance at source–detector separations close to one transport mean free path," J. Opt. Soc. Am. A **16,** 2935–2945 (1999).
38. A. Kienle and M. S. Patterson, "Determination of the optical properties of semi-infinite turbid media from frequency-domain reflectance close to the source," Phys. Med. Biol. **42,** 1801–1819 (1997).
39. T. Kuboki, K. Suzuki, K. Maekawa, M. Inoue-Minakuchi, C. O. Acero Jr, Y. Yanagi, T. Wakasa, K. Kishi, H. Yatani, and G. T. Clark, "Correlation of the near-infrared spectroscopy signal with signal intensity in T_2-weighted magnetic resonance imaging of the human masseter muscle," Arch. Oral. Biol. **46,** 721–727 (2001).
40. E. L. Hull, D. L. Conover, and T. H. Foster, "Carbogen-induced changes in rat mammary tumour oxygenation reported by near infrared spectroscopy," Br. J. Cancer **79,** 1709–1716 (1999).
41. H. Liu, Y. Song, K. L. Worden, X. Jiang, A. Constantinescu, and R. P. Mason, "Noninvasive investigation of blood oxygenation dynamics of tumors by near-infrared spectroscopy," Appl. Opt. **39,** 5231–5243 (2000).
42. R. G. Steen, K. Kitagishi, and K. Morgan, "*In vivo* measurements of tumor blood oxygenation by near-infrared spectroscopy: immediate effects of pentobarbital overdose or carmustine treatment," J. Neuro-Oncol. **22,** 209–220 (1994).
43. S. S. Gambhir, H. R. Herschman, S. R. Cherry, J. R. Barrio, N. Satayamurthy, T. Toyokuni, M. E. Phelps, S. M. Larson, J. Balatoni, R. Finn, M. Sadelain, J. Tjuvajev, and R. Blasberg, "Image trangene expression with radionuclide image technologies, Neoplasa **2,** 118–138 (2000).